ADVANCED FUNCTIONAL MATERIALS
www.afm-journal.de

Oxidation-Degradable Resins for 3D-Printing of Cell-Responsive Biomaterials

*Reinaldo L. Dos Santos, Wesley Wynn, Lindsey Marquez, Ejajul Hoque, Karina A. Bruce, Benjamin M. Yavitt, Greg M. Harris, and John R. Martin**

Additive manufacturing, or 3D printing, has emerged as a powerful tool for rapidly generating tissue engineering constructs with complex architectures. While hydrolysis-sensitive polyesters are most commonly used to 3D print these scaffolds, once implanted, these materials often degrade prematurely before tissue regeneration is achieved. To address these limitations, this study introduces new oxidation-sensitive resins that can be 3D-printed into implants designed to selectively degrade when exposed to cell-produced reactive oxygen species (ROS). Although these ROS-triggerable polymers have shown promise for matching tissue growth with implant degradation, they have yet to be adapted into simple, low-cost formulations compatible with commercial 3D printers. Here, UV-photopolymerizable, ROS-sensitive resins are created from synthesized thioketal (TK) dithiols and commercial alkene crosslinkers. A novel small-scale screening method is developed to determine each resin's optimal concentrations of photo-initiator and inhibitor. All TK resins support fine-detail 3D printing, exhibit negligible in vitro cytotoxicity, and display tunable mechanical properties and oxidative sensitivity based on their respective chemistries. Finally, 3D-printed TK scaffolds implanted subcutaneously in rats undergo significant biodegradation over 4 weeks and foster more rapid tissue infiltration than 3D-printed polyester controls. These findings highlight the potential of oxidation-sensitive resins for creating cell-responsive, tissue-regenerating medical implants with complex architectures.

1. Introduction

Additive manufacturing (AM), more commonly known as 3D printing, has emerged over the past few decades as a powerful tool for engineering medical implants with complex architectures for applications in regenerative medicine.[1] There have been many AM methods developed since this technology's initial description by Charles Hull,[2] including fused deposition modeling (FDM) and vat photopolymerization (VP) for the 3D printing of polymeric materials. Within the medical space, polymeric AM has been used for many applications; to date, the most common use case for this technique combines 3D printing with scanning technologies such as computed tomography or magnetic resonance imaging to 3D print patient-specific tissue models to use in surgical planning.[3] These techniques have also been used to create "biostable" medical implants that are meant to last for many years when placed in the body.[4] However, this technology is especially promising for the development of resorbable tissue engineering scaffolds[5] since AM can ideally provide personalized implants to fit an irregularly sized tissue injury, can create complex and inter-connected pore structures that are difficult to achieve with non-AM methods,[6] and can use biodegradable materials to naturally remove an implant from the body.[7] Within the field of tissue engineering, the development of biodegradable scaffolds that provide mechanical support to a wound area, guide tissue regeneration, and improve disease state outcomes has been a center of focus in recent efforts.[8]

Both FDM and VP methods have been used to 3D print polymeric tissue engineering scaffolds in recent reports.[9,10] FDM is the most common AM method for biodegradable polymers, but can only utilize extrudable thermoplastic materials such as polycaprolactone (PCL), poly(lactic-*co*-glycolic) acid (PLGA), and poly(dioxanone) (PDO). These materials have been used to develop 3D-printed drug delivery systems,[11,12] scaffolds for tissue engineering and regenerative medicine,[13–15] and surgical guidance tools.[16,17] VP uses spatially controlled UV illumination and photopolymerizable liquid resins to build 3D objects in a layer-by-layer manner to achieve significantly finer layer resolutions compared to FDM.[18] Though VP printing requires slightly more expensive hardware and feedstock materials than FDM, the UV-triggerable liquid resins used in these methods offer a more extensive choice of achievable material properties.[19]

R. L. D. Santos, W. Wynn, L. Marquez, K. A. Bruce, G. M. Harris, J. R. Martin
Biomedical Engineering
University of Cincinnati
Cincinnati 45221, USA
E-mail: marti7j3@ucmail.uc.edu

B. M. Yavitt, G. M. Harris
Chemical Engineering
University of Cincinnati
Cincinnati 45221, USA

E. Hoque
Mechanical and Materials Engineering
University of Cincinnati
Cincinnati 45221, USA

The ORCID identification number(s) for the author(s) of this article can be found under https://doi.org/10.1002/adfm.202522208

DOI: 10.1002/adfm.202522208

Digital light processing (DLP) is a popular VP printing method that leverages a UV projection of part cross-sections to crosslink polymer layers on a build plate all at once for increased printing speeds.[18,20] Despite the advantages of VP techniques over FDM for generating medical implants with superior printing quality and more diverse properties, relatively few VP-compatible biodegradable photopolymers have been developed to date due to tradeoffs between resin printability, mechanical performance, and degradability.[21] Therefore, developing photoresins that can be 3D printed into robust biodegradable implants represents a significant opportunity in this field.

Due to their ease of synthesis and successful deployment in many other medical applications, synthetic polyesters have been the most popular choice of material precursors for developing biodegradable, VP-compatible photopolymers.[21] However, conventional PCL, PLGA, and PDO polyesters can suffer significant shortcomings as resorbable implants. Biodegradation of these materials is primarily mediated by non-specific hydrolytic degradation of ester bonds in their polymer backbone.[22,23] Tuning the degradation rates of polymeric implants for specific medical applications remains a key engineering design criterion for these AM-compatible materials.[23]Accordingly, the biodegradation lifetimes of standard polyesters are highly tunable (PCL > 24 months, PLGA 2-6 months, PDO 6–8 months).[24] However, if scaffold degradation rates are not properly matched with the pace of tissue regeneration, this can result in incomplete tissue healing from prematurely resorbed implants.[25] To this end, "smart" polymers that react to specific biological stimuli, including enzymes, pH, or reactive oxygen species (ROS),[26] have been extensively investigated in biomaterials research but have seen more limited impact in AM technology development.[27] Therefore, the goal of this work was to develop simple, low-cost, biologically-responsive polymeric materials that are compatible with commercial VP 3D printing systems and can generate medical implants that undergo selective cell-mediated resorption in vivo.

In the area of environmentally responsive polymers, new materials have recently emerged that feature specific biodegradation in response to cell-generated ROS.[28,29] In the body, ROS are present in multiple forms and play key roles in tissue regeneration after damage.[29–31] ROS production increases substantially during inflammation and promotes immune cell migration toward the site of inflammatory signaling.[32] These oxidants serve a dual role by mediating either beneficial or detrimental effects depending on the biological circumstances. At low concentrations, ROS can induce cell differentiation,[33] activate key regenerative pathways,[29] and induce neovascularization.[30,32] At higher concentrations and for prolonged timelines, however, ROS can become a detriment to tissue regeneration by inducing oxidative stress, which damages cells[33] and fosters the chronic inflammation that underlies various pathologies.[30,34,35] Seeking to target these inflamed and highly oxidative tissues with biomaterial-based therapies, many ROS-responsive polymers have been developed over the past two decades, including polysulfides, poly(oxalates), phenylboronic esters, and thioketals (TKs).[29] Since their introduction in 2010,[36] thioketals have become an increasingly popular chemistry for creating these triggerable platforms due to their ease of synthesis, stability in non-oxidative conditions, and susceptibility to a relatively wide range of ROS molecules.[29] Consequently, TK linkers have been incorporated into many polymeric biomaterials to create ROS-responsive nanoparticles,[36] tissue engineering scaffolds,[37] bone substitutes,[38–40] injectable hydrogels,[41] and layer-by-layer drug coatings.[42] These previous TK systems are all nearly inert in aqueous conditions but display dose-responsive activation with ROS. Despite the promise of TK chemistries, they have not yet been developed into simple[43] and low-cost formulations that are compatible with commercial 3D printers.

The overall goal of this work was to generate 3D-printable polymeric biomaterials that selectively biodegrade in response to cell-generated ROS. DLP 3D printing (schematic in **Figure 1A**) was chosen as the material fabrication method of choice since this technology uses liquid resins, which can achieve a wider variety of material properties than the thermoplastics used in FDM printing.[19] Here, a family of resins were formulated with TK linkers and used to 3D-print polymeric scaffolds with tunable mechanical properties, modifiable degradation kinetics, and controlled in vivo resorption.

2. Results and Discussion

2.1. TK Resin Formation

To create a family of TK-based liquid resins amenable to UV-triggered crosslinking and DLP 3D printing, varying TK dithiols (Figure 1B) were synthesized and combined with two different alkene-terminated crosslinkers (Figure 1C) alongside resin-specific amounts of photo-initiator and photo-inhibitor (Figure 1D). These resins employed photo-sensitive thiol-ene chemistries due to this reaction's rapid progression, high efficiency, and uniform polymer network formation.[19] Using the non-toxic dithiol monomer 3,6-dioxa-1,8-octanedithiol (DOT),[44,45] two thiol-terminated TK linkers were synthesized using previously described methods[37] as confirmed by nuclear magnetic resonance (NMR) spectroscopy, shown in Figure S1 (Supporting Information). Molecular weights of the respective TK linkers were modulated by manipulating stoichiometric quantities of the DOT monomer and 2,2-dimethoxypropane (DMP) during polymerization. By forming TK oligomers using a 2:1 or 1:0.9 molar ratio of DOT to DMP, a short-chain TK (SCTK) and long-chain TK (LCTK) were respectively formed (Figure 1B; Table S1, Supporting Information). Two commercially available alkene-terminated crosslinkers featuring methacrylate (MA, trimethylolpropane trimethacrylate) or allyl ether (AE, pentaerythritol allyl ether) tri-functional end groups were utilized to compose these varying resins (Figure 1C). Methacrylates and allyl ethers both efficiently bond with thiols groups under mild photoinitiation,[46] leaving these materials well-suited for use in VP 3D printing. Additionally, these MA and AE crosslinkers are both relatively inexpensive and widely commercially available, making them particularly attractive for translational scale-up.

In this work, three TK resin formulations were generated as denoted in Figure 1E: the SCTK dimer was combined with either AE or MA to generate SCTK-AE and SCTK-MA resins, while the LCTK oligomer was combined with MA for a LCTK-MA resin. LCTK-AE resins were attempted but ultimately not pursued because they did not form robust polymerized products after UV exposure. The type 1 photo initiator phenyl bis(2 4 6-trimethylbenzoyl)-phosphine oxide (BAPO, Figure 1D), also

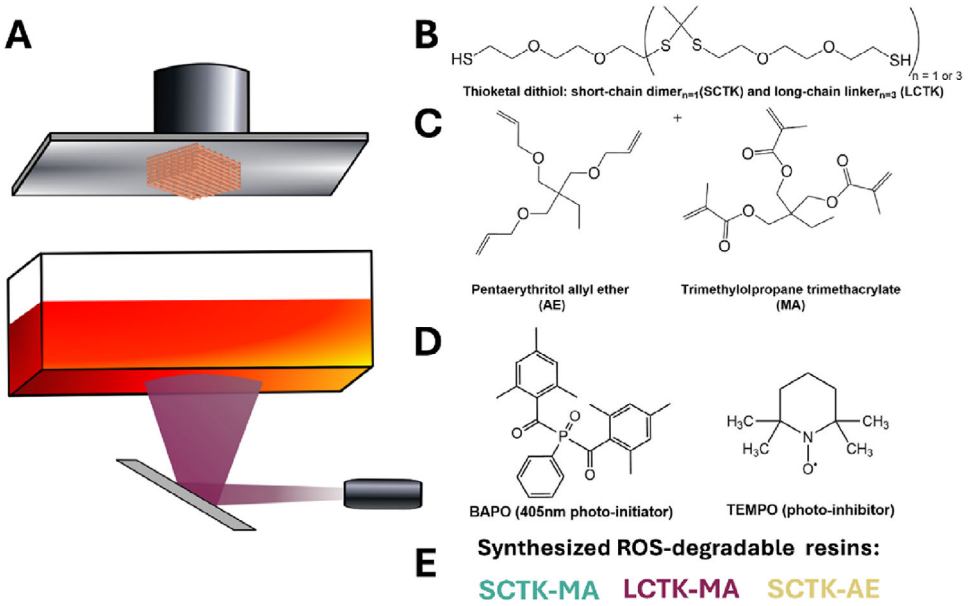

Figure 1. A) Schematic of DLP 3D printing via UV-triggered crosslinking of thiol-ene resins. These low viscosity resins are formulated from combinations of B) oxidation-sensitive, low molecular weight TK dithiol oligomers, C) commercially available -ene terminated crosslinkers, and D) the photo-initiator BAPO and photo-inhibitor TEMPO. E) The three formulated resins are denoted throughout with consistent names and color schemes based on their respective thiol and -ene crosslinker constituents.

known as Irgacure 819, was chosen as the thiol-ene UV crosslinking catalyst in all three resins. This photo-initiator has strong photo-initiation in the near UV–Vis light range used by many commercial 3D printers,[47] is minimally toxic,[48] and has been successfully used in thiol-ene photopolymerizations.[49] The radical scavenger TEMPO (Figure 1D) was also added into all three TK resins to limit unwanted polymerization and improve the spatial resolution of printed structures. TEMPO has been previously utilized to temper photo-radical polymerizations[50] and as an additive in DLP resins.[51] While TEMPO has been shown to elicit some cellular toxicity at concentrations above 3 mM, lower concentrations such as those used here are biocompatible.[52]

2.2. Resin Optimization Using Small-Scale Rapid Prototyping

Free radical-producing photo-initiators are used to induce polymerization for thiol-ene materials[46] and for other chemistries commonly employed in DLP 3D printing.[18] However, for biomedical applications where the presence of these potentially toxic additives can hamper an implant's biological performance, limiting the concentration of photo-initiators is a chief concern.[53] Unfortunately, there are few available methods for determining a minimal dose of photo-initiator / photo-inhibitor within a 3D printing resin that can still achieve proper XY axis resolution of UV-patterned structures. To assess the fidelity of 3D-printed parts, the most common technique involves printing an easily measured geometry (such as a cube structure) and comparing achieved part sizes with their nominal input shape.[54] While this method has proven useful in many 3D printing applications, it suffers from some inherent limitations. Large resin volumes are typically needed for DLP 3D printing, which becomes challenging when exploring novel formulations created with non-commercially available materials. Additionally, rapidly prototyping many formulations of photo-initiator and inhibitor is expensive, time-consuming, and generates large amounts of chemical waste. Therefore, a novel method was developed here to rapidly screen small volumes of varying resins for UV photopolymerization outcomes based on selective spatial irradiation. As outlined in **Figure 2A**, small 0.1 mL quantities of TK resins featuring a 1% molar equivalent dose of photo-initiator (BAPO) and varying doses of photo-inhibitor (TEMPO) were first deposited onto glass slides. Samples were then placed onto a UV array where only half of the resin droplet was directly exposed to UV. UV illumination was performed for 10-15s to simulate one layer of exposure in a larger vat resin, and this process was then repeated 50 times to mimic the on-off UV irradiation seen in layer-by-layer 3D printing in the Z-axis (Figure 2B). After each resin droplet had been irradiated for the desired number of cycles, the hardened sample was washed with acetone to remove any unpolymerized material. As shown in representative images in Figure 2C, resin formulations that presented no crosslinking in non-UV irradiated space were chosen as lead-candidate formulations and carried forward in subsequent studies. As given in **Table 1**, the makeup of chosen SCTK-MA, LCTK-MA, and SCTK-AE resins all displayed negligible over-crosslinking when generating these UV-hardened samples. BAPO concentrations of 1% molar equivalent were used in all formulations to limit any potential cytotoxicity concerns.

2.3. Characterization of TK Resins for Selective Polymerization and Stability

Though thiol-ene photo-crosslinked materials are known to feature relatively uniform network structures upon formation,[55]

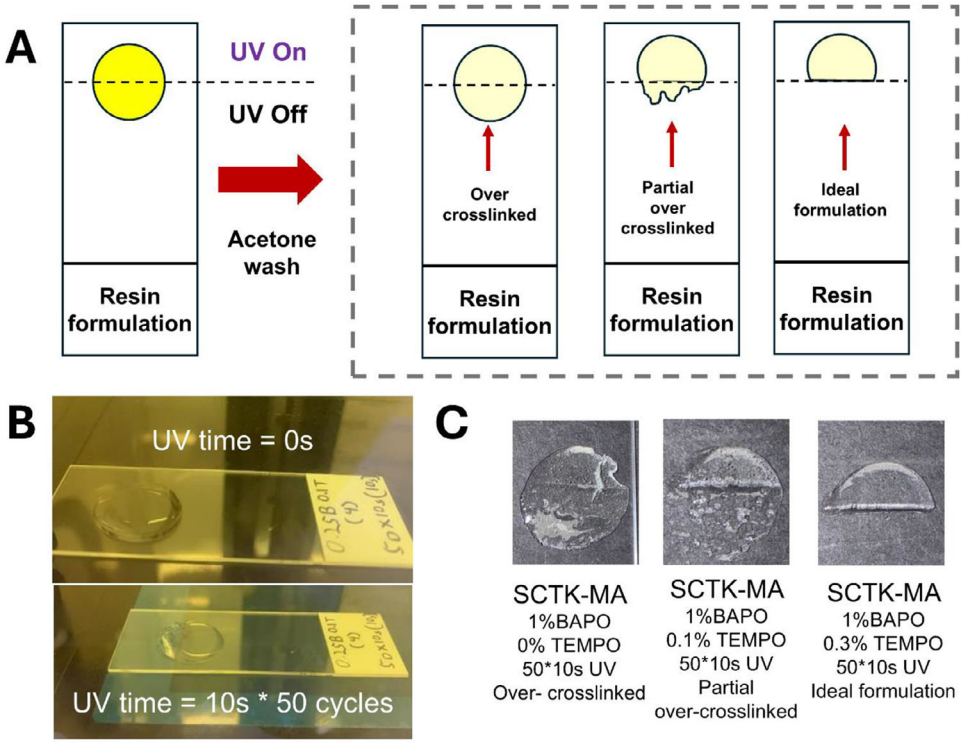

Figure 2. A) Illustration of small-scale resin screening methods using 0.1 mL resin volumes on microscope slides. B) Half of the resin on the glass slide was irradiated with UV for 50 cycles, while the other half of the droplet was not. C) Following a solvent wash, the extent of material crosslinking in non-irradiated material was qualitatively assessed.

alkene-terminated monomers have been known to homopolymerize with exposure to radicals.[56] Therefore, the three TK thiol-ene resins were characterized using attenuated total reflectance Fourier transform infrared spectroscopy (ATR-FTIR) to confirm selective thiol-ene conjugation upon UV irradiation and not unwanted ene-ene crosslinking (Figures S2 and S3, Supporting Information). As shown in Figure S2 (Supporting Information), the specific alkene peak in both the MA and AE crosslinkers was essentially unchanged after UV irradiation, and no physical crosslinking was observed, indicating that homopolymerization was negligible. In additional ATR-FTIR evaluations, the lead candidate SCTK-MA, LCTK-MA, and SCTK-AE resins all had their respective thiol and alkene peaks substantially eliminated following UV exposure as shown in Figure S3 (Supporting Information). The lack of residual thiol or alkene peaks further confirms the near-complete conversion of these functional groups upon photopolymerization. As shown in Figure S4A (Supporting Information), photo-rheology was also employed to demonstrate the rapid and drastic increase in material stiffness of representative SCTK-AE resin samples upon irradiation at 405 nm.

Photo-rheology was further used to confirm the stability of the TK linker during the DLP printing process, which creates free radicals to induce material crosslinking. When mixed with the radical-generating BAPO, the SCTK displayed no evidence of TK bond degradation (i.e., loss of viscosity) during an excessive 2 min irradiation session with 405 nm light (Figure S4B, Supporting Information). This demonstrated that the radical-generating photoactivation by 1% BAPO during 3D printing is sufficient to induce thiol-ene crosslinking but not enough to significantly damage the TK bonds over these relatively short time spans. The stability of these resins was also validated by measuring their viscosities after 30 days of storage in dry UV-resistant bottles at 4 or 25 °C, with all three formulations showing negligible differences from initial values (Figure S4C, Supporting Information).

2.4. Optimization of 3D Printing Parameters for TK Resins

With the three lead candidate TK resin recipes established (Table 1), corresponding 3D printing parameters for each formulation were next determined to ensure compatibility with a commercially-available Anycubic Photon Mono 4K 3D printer. This machine features a 405 nm light source and 1.6 mW cm^{-2} irradiation power output as determined from an optical power detector. A print layer height of 100 µm was chosen for proof-of-concept testing to establish the irradiation time per layer for each

Table 1. Lead candidate TK resin formulations (100 g scale) taken from small-scale prototyping experiments.

Resin	TK [g]	Tri-functional ene [g]	BAPO [g]	TEMPO [mg]
SCTK-MA	63.9	36.1	1.34	50
LCTK-MA	76.3	23.7	0.88	33
SCTK-AE	70.1	29.9	1.46	110

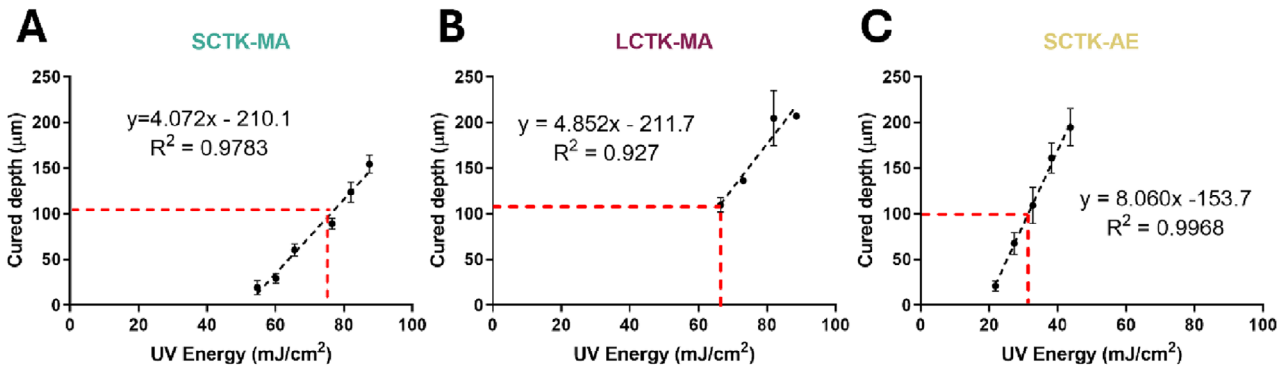

Figure 3. Determination of resin cured depth (C_d) values as assessed from photo-rheology. By modifying UV exposure time for A) SCTK-MA, B) LCTK-MA, and C) SCTK-AE resin samples, the required UV energy needed to achieve a 100µm-thick cured layer for each resin (indicated by red dashed lines) was obtained from measurements of the normal force (Figure S5, Supporting Information) from crosslinked samples.

respective resin. In VP, photo-curable resins are irradiated with UV to induce crosslinking in a spatially controlled manner.[20] Paul Jacobs developed the working curve equation[57] (Jacobs equation, Equation 1) relating photocurable resin UV exposure (E) to cured depth (C_d)

$$C_d = D_p \ln\left(\frac{E}{E_c}\right) \quad (1)$$

where depth of penetration (D_p) and critical exposure (E_c) are unique material properties needed to 3D print with photo-resins. The working curve relates UV exposure to cured layer thickness, thus allowing for precise control of polymerization required in layer-by-layer 3D printing techniques.[57] Methods for measuring cured depth were developed by Jacobs[57] and others,[58] though these methods necessitated the use of calipers and micrometers for measuring C_d and intrinsically introduced significant user error between trials. While cured depth is essential for VP techniques, no standardized methods for determining this value exist.

Rau et al.[59] recently developed a photo-rheological method which utilizes gap distance and normal force thresholds for automated and precise determination of the working equation for photo-resins. This method was utilized to determine D_p and E_c for the three TK resins developed in this study. Figure S5 (Supporting Information) shows a characteristic gap-force curve where UV exposure times (E in Equation 1) were varied to determine the corresponding thickness of crosslinked resin as determined from a measured normal force threshold of 2N. These values were used to create best-fit working curves for SCTK-MA, SCTK-AE, and LCTK-MA resins that relate UV energy input to amount of material crosslinking (**Figure 3**). Using a thickness of 100 µm per layer, the working curves for each resin were used to determine the layer time exposure needed to achieve full material crosslinking based on the 1.6 mW cm^{-2} of UV energy output from the Anycubic 3D printer. These values are listed in **Table 2**.

2.5. Physical Characterization of 3D-Printed Samples Generated from TK Resins

With resin chemistries established, the three TK formulations were used to 3D print different constructs. Once parts were 3D printed, a typical workflow had samples washed in isopropyl alcohol to remove unreacted resin, and then performing a final post-cure using an Anycubic Wash and Cure 2.0 system. Model cylinder samples (0.5 mm diameter, 1 mm height) were 3D printed and used to determine the physical properties of 3D-printed constructs from the respective TK resins. Sol-fraction values were first determined by measuring the mass of sample retained after soaking prints in the resin-dissolving solvent dichloromethane. As shown in **Table 3**, prints from all three resins had less than 3% mass loss after extracting their soluble fraction. This indicated that all three resins were well-formulated and that the amounts of potentially toxic leachable agents from these implants were relatively low. The molecular mesh sizes of these materials were determined from solvent swelling data and the Flory–Rhener equation,[60] and indicated that final samples ranged from lower to higher mesh sizes for the respective formulations (SCTK-MA < LCTK-MA < SCTK-AE) as shown in Table 3. The SCTK-AE's larger mesh size is likely due to the mix of di-, tri-, and tetra-functionalized allyl ether crosslinkers that are present in the commercial pentaerythritol allyl ether obtained from the supplier. Though the allyl ether groups are well-matched with thiols in the SCTK-AE resins as confirmed with FTIR (Figure S3C, Supporting Information) and sol-fraction data (Table 3), it is likely the significant fraction of diallyl ether molecules within the resin

Table 2. Printing parameters of TK resins for an Anycubic DLP 3D printer.

Resin	Layer height [µm]	UV energy [mJ cm^{-2}]	Layer time [s]
SCTK-MA	100	76.1	47.5
LCTK-MA	100	64.2	40.1
SCTK-AE	100	31.5	19.7

Table 3. Physical properties of printed TK scaffolds assessing water contact angle, mesh size, and sol-fraction.

Resin	Sol-fraction [%]	Mesh size [nm]	Water contact angle [°]
SCTK-MA	2.4 ± 0.5	1.7 ± 0.2	31 ± 2.6
LCTK-MA	2.2 ± 1.5	2.7 ± 0.2	45 ± 1.6
SCTK-AE	2.1 ± 1.5	4.4 ± 0.1	57 ± 2.0

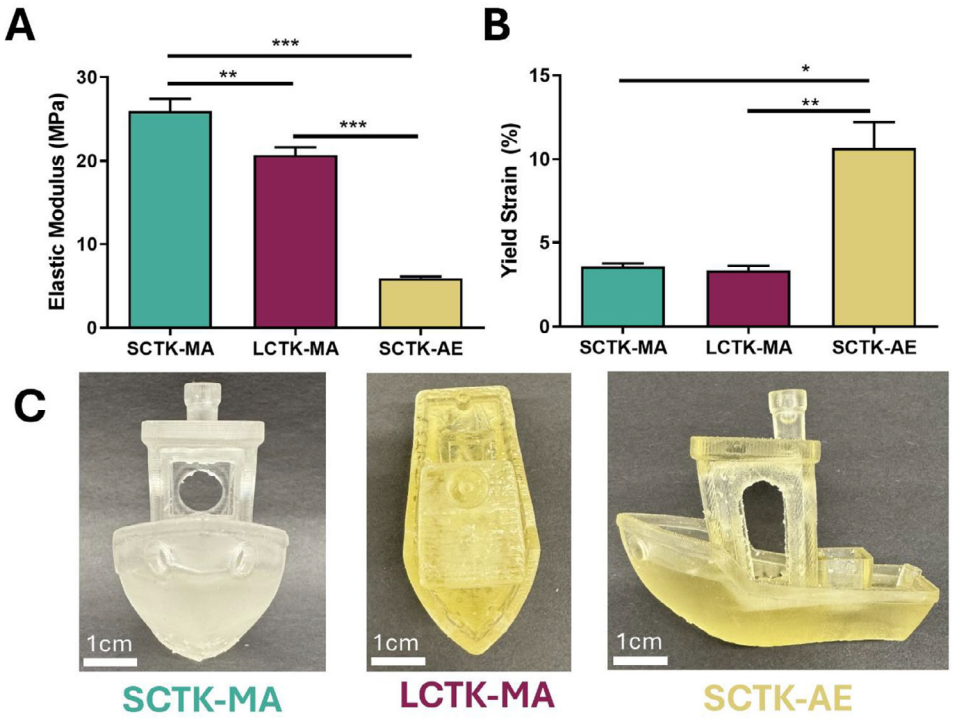

Figure 4. Tensile properties of samples 3D printed from TK resins demonstrated differential values for A) elastic modulus and B) yield strain based on the respective resin formulation chemistry. C) Proof-of-concept printing of benchmark "Benchy" tugboat models established these resins' capacities for generating complex geometries upon 3D printing.

caused the looser polymer networks in this formulation. Contact angle testing was also performed on 3D-printed samples and demonstrated that SCTK-MA resins generated the most hydrophilic final materials while SCTK-AE resins produced the most hydrophobic (Table 3).

Understanding the range of achievable properties in 3D-printed constructs is imperative when utilizing these materials in medical applications.[61] Implanted biomaterials necessitate specific mechanical properties depending on what tissue the material is interfacing with[62] and the desired function of the implant. Therefore, tensile properties of 3D-printed dog bone samples formed from the three TK resins were tested according to ASTM D638 protocols.[63] Specimens ($n = 5$) were 3D printed, washed, post-cured, and incubated in phosphate-buffered saline (PBS) for 5 days before performing tensile testing to assess "wet" mechanical properties. As shown in **Figure 4**A,B, an inverse relationship was illustrated between the elastic modulus and yield strain of the 3D printed samples from the three TK resins. SCTK-MA specimens possessed the highest elastic modulus (Figure 4A) but the lowest yield strain (Figure 4B). LCTK-MA samples had expectedly lower stiffness values than SCTK-MA analogues (Figure 4A) since the higher molecular weight LCTK decreased the crosslink density and correspondingly increased network mesh size (Table 3). Conversely, SCTK-AE specimens possessed lower stiffness but greater ductility compared to the MA-based resins, as shown in Figure 4A,B. Measured ultimate stress, yield stress, and toughness parameters featured similar trends, as SCTK-MA prints displayed the highest ultimate and yield stress values, while toughness was greatest in printed SCTK-AE samples (Figure S6, Supporting Information). For all three resin formulations, the determined molecular mesh size (Table 3) strongly correlated with experimentally determined mechanical properties. These findings demonstrate the ability to vary the strength and ductility of 3D-printed TK implants by introducing small changes to the resin constituents' molecular architectures. As shown in Figure 4C, the three respective TK resins were also 3D printed into "Benchy" tugboat models to confirm these materials' ability to form complex 3D shapes.

2.6. In Vitro Oxidative Degradation of 3D-Printed TK Materials

TK-based biomaterials have been shown to selectively degrade in the presence of cell-produced ROS[29,37,38] and offer a biologically-responsive alternative to passively-degrading medical implants. Therefore, characterizing the oxidative degradation of TK resin scaffolds was imperative for this material system. The three respective TK resins were used to 3D-print model cylindrical samples before measuring their mass loss after incubation in non-oxidative conditions or in supra-physiologic ROS concentrations that simulate in vivo oxidative degradation at an accelerated rate.[64] Printed materials were immersed in non-oxidative PBS or in accelerated oxidative media containing 2% or 20% concentrations of the model ROS molecule hydrogen peroxide (H_2O_2). To relate these in vitro ROS doses to in vivo degradation kinetics, past TK-urethane scaffolds implanted in rats were resorbed at rates comparable to in vitro samples incubated in 0.2% H_2O_2 media.[37] As shown in **Figure 5**, TK scaffolds from all three resin

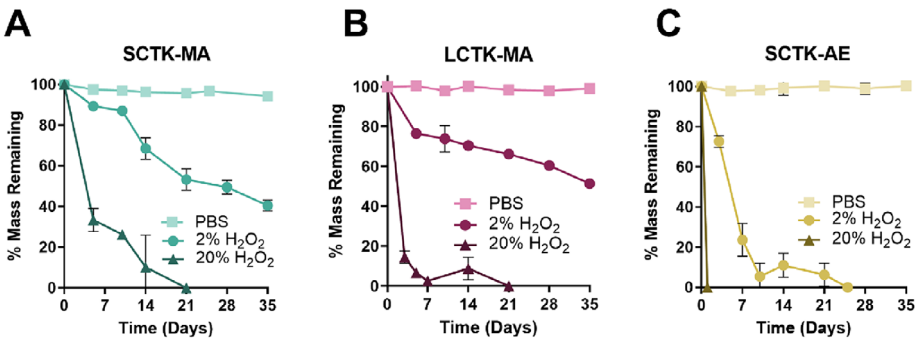

Figure 5. Selective in vitro degradation of 3D-printed TK scaffolds in accelerated oxidative conditions. Model samples printed from A) SCTK-MA, B) LCTK-MA, and C) SCTK-AE resins were highly stable in purely aqueous media but underwent dose-dependent degradation when incubated in escalating doses of H_2O_2. The SCTK-AE prints underwent the most rapid ROS-mediated breakdown compared to the other two formulations.

formulations demonstrated negligible mass loss over time when incubated in PBS. However, TK samples were significantly broken down in H_2O_2 media at dose-dependent rates (Figure 5) and had decreased mechanical stiffness after three days of ROS exposure (Figure S7, Supporting Information). This degradation behavior agrees with previous reports of TK biomaterials being inert in aqueous conditions but undergoing dose-dependent degradation in ROS-rich media.[29,37,38]

Interestingly, scaffolds fabricated from the different TK resins underwent varying rates of ROS-mediated degradation. Printed SCTK-MA materials (Figure 5A) showcased the slowest rate of degradation, LCTK-MA samples degraded slightly faster (Figure 5B), and SCTK-AE scaffolds degraded most quickly at corresponding ROS doses (Figure 5C). Unlike previously reported TK implants where degradation kinetics were governed most strongly by material hydrophilicity,[45] the degradation behavior of these 3D-printed TK samples (Figure 5) does not align with these formulations' hydrophilicity values in Table 3. However, the mesh size values and corresponding mechanical properties (Figure 4A,B) do correlate with ROS-mediated degradation kinetics, as the least-stiff SCTK-AE samples underwent the most rapid breakdown in vitro. These data indicate that modifying the polymer network density, either by incorporating higher molecular weight constituents (LCTK versus SCTK) or less branched crosslinkers (fraction of diallyl ethers in the SCTK-AE resin), allows for controlled tuning of the oxidation-responsive degradation of these TK scaffolds.

2.7. Cytotoxicity of 3D-Printed TK Materials

Scaffold samples printed from the three respective TK resins and a commercially available biomedical resin were assessed for in vitro cytotoxicity using an elution-based toxicity test adapted from ISO 10993-5. The Biomed Elastic 50A Resin (Formlabs, Somerville, MA) was chosen as a control material since it is a non-degradable, biostable resin commonly recommended for material applications with long-term skin contact or short-term mucosal membrane contact. Cylinders were 3D printed from the four respective resins, washed, post-cured, and incubated in full cell media for 24 h. The treated media samples were administered to MC3T3-E1 pre-osteoblast cells in full and diluted quantities for 24 h before measuring the number of live cells using a CellTiter Glo assay. As shown in **Figure 6**, no statistically significant differences in viability were observed between cells treated with scaffold-conditioned media and the control no-treatment group. These negligible cytotoxicity results were anticipated since both the TK and 50A resins generated well-formed prints with low sol-fraction values (Table 3) that were unlikely to elute substantial unreacted monomer. These experiments did not assess the toxicity of potential TK or 50A degradation products since neither resin was expected to degrade in aqueous cell media over 24 h. However, the limited toxicity of TK biomaterials and their degradation products has been well-established in previous reports[38,65] and generally aligns with these findings.

2.8. Generation of 3D-Printed Tissue Scaffolds with Uniform Grid Architectures

To generate porous tissue engineering scaffolds with uniform and reproducible structures, implants featuring a grid architecture and interconnected channels were successfully 3D printed from the three TK resins and a commercial poly(dioxanone) (PDO) control material as shown in light microscopy images in **Figure 7**. The roughly 10 mm-wide and 0.8 mm-thick implants

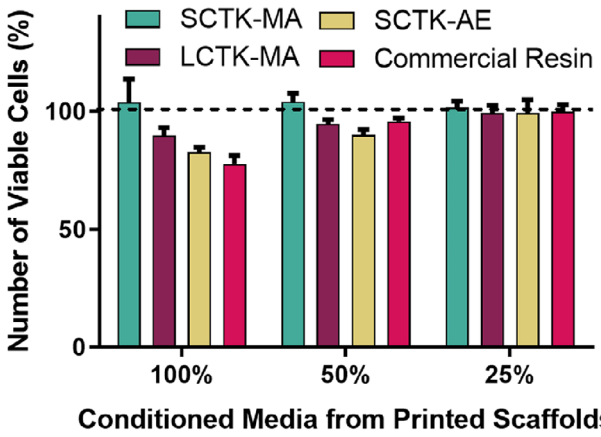

Figure 6. Elution cytotoxicity assay in MC3T3-E1 pre-osteoblast cells to compare toxicity of parts printed from TK resins against samples printed from a commercially-available biostable resin. The number of viable cells for no-treatment control cells is indicated by the dashed line at 100%.

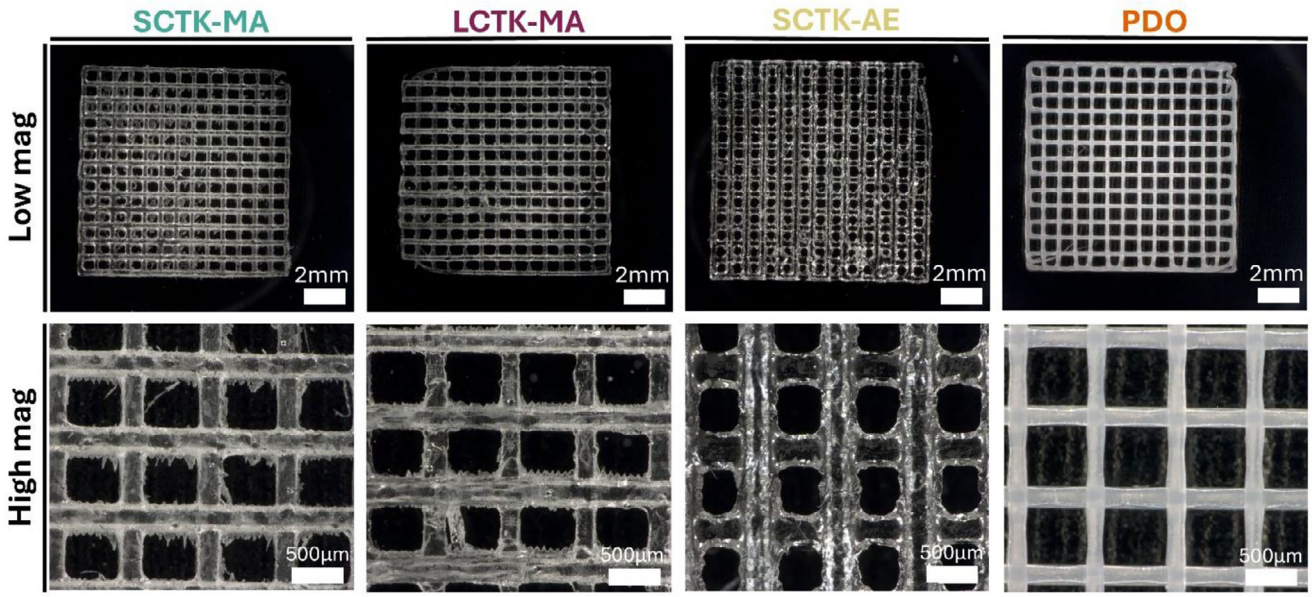

Figure 7. Light microscopy images of uniform, grid-architecture tissue engineering scaffolds 3D printed from the three TK photoresins and a control PDO polyester FDM filament.

were designed with 200 µm strut widths, interconnected 600 µm-wide pores, and over 70% volumetric porosity as outlined in Figure S8 (Supporting Information). These highly porous scaffolds were devised to ensure adequate tissue infiltration once implanted in vivo, since pore sizes in this size range have been shown to promote high levels of cellular infiltration in biomaterial implants.[66,67] Because very few hydrolytically-degradable resin materials designed for medical applications have been successfully developed in the research space, much less as marketable products,[21] a commercially-available FDM filament made from the thermoplastic polyester PDO was chosen for fabricating control scaffolds. PDO undergoes relatively fast degradation in vivo compared to other polyesters (resorption within a few months[68]), which corresponded well with biodegradation rates seen in similar porous TK implants.[37]

The three TK resins were used to fabricate respective TK scaffolds on a commercial DLP 3D printer (Anycubic Photon Mono 4K) while the PDO scaffolds were fabricated using a commercial FDM 3D printer (Prusa i3 MK3). This particular scaffold geometry was created to allow for 3D printing of matching samples from either DLP or FDM equipment. The Prusa printer employed a 200 µm extrusion nozzle, which determined the minimum strut size that was achievable, while each 200µm-thick strut layer was printed in a continuous extrusion step to limit the introduction of defects. In preliminary testing, it was found that the original TK resin formulations listed in Table 1 were suffering from over-crosslinking during DLP fabrication and that final prints did not contain well-defined pores. Therefore, concentrations of the TEMPO photo-initiator were increased in all three TK resins to ensure reliable generation of open-pore scaffolds with micron-scale features, as shown in Figure 7. The constituents of these modified resins are listed in Table S2 (Supporting Information), and the slightly modified 3D printing parameters are listed in Table S3 (Supporting Information). As shown in Figure S9 (Supporting Information), a print efficacy analysis was performed on final scaffolds from all four material formulations to compare the fidelity of printed implants with their prescribed model geometries. All four materials achieved relatively on-target strut width values in final prints (Figure S9A, Supporting Information) and low levels of strut size variability (Figure S9B, Supporting Information). SCTK-AE resins featured the largest dimensional deviation for printed strut width by achieving ≈40% print accuracy, while the LCTK-MA resin achieved 90% print fidelity (Figure S9A, Supporting Information). These levels are roughly in line with similar DLP examples from literature, which achieved dimensional accuracies between 53% and 90% when printing micron-scale features.[69,70] The photo-polymerized TK scaffolds do appear somewhat rougher than the PDO samples, as shown in Figure 7, though this morphology is seen in similar thiol-ene photo-resins[71] and is likely due to low levels of non-specific over-crosslinking common with this chemistry.

2.9. In Vivo Biodegradation, Tissue Infiltration, and Cellular Responses of 3D-Printed TK Scaffolds

SCTK-MA, LCTK-MA, SCTK-AE, and PDO grid scaffolds were fabricated, sterilized, and subcutaneously implanted in Sprague Dawley rats (n = 3 males, n = 3 females per timepoint). Tissue/scaffold samples were harvested at two and four weeks after implantation and processed for histology with hematoxylin & eosin (H&E) staining (**Figure 8A**) to assess tissue infiltration into the porous grid structure (Figure 8B), scaffold degradation over time (Figure 8C), and the response of surrounding tissues to these novel materials (Figure 9). As shown in representative histology images in Figure 8A, all four scaffold formulations fostered substantial cellular infiltration throughout the entire implant architecture by two weeks and had increasing tissue

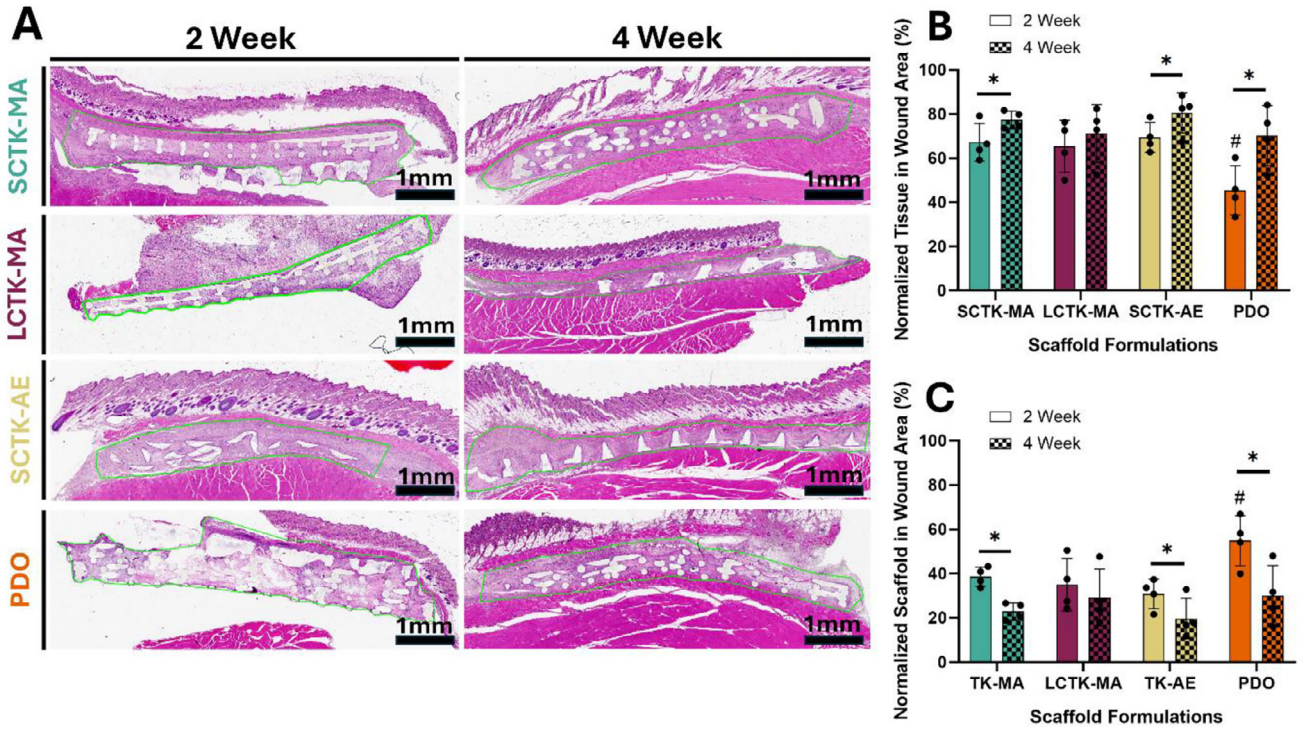

Figure 8. In vivo response of 3D-printed TK and PDO control scaffolds subcutaneously implanted in Sprague Dawley rats. A) Representative H&E-stained sections of scaffold/tissue explants harvested after two- and four-week implantation periods demonstrate robust tissue infiltration into all four scaffold formulations (each scaffold's "wound area" denoted by a green ROI). Quantification of B) tissue and C) scaffold levels within selected ROIs demonstrate that both TK and control implants hosted increasing cellular in-growth from two to four weeks and significantly biodegraded over time. However, tissue infiltration into the TK scaffolds was significantly higher than the PDO controls at the early two-week timepoint. (at least $n = 4$ samples per treatment at each timepoint, $^{*}p < 0.05$ comparing week 2 to week 4, $\#p < 0.05$ comparing PDO against all TK treatments within the same timepoint).

development from two to four weeks. The amount of tissue (Figure 8B) and scaffold (Figure 8C) present within each implant's "wound area" region of interest (ROI) were quantified using a custom-built image segmentation script built in Python. All three TK formulations demonstrated significantly greater tissue infiltration than PDO scaffolds at the two-week timepoint (Figure 8B), and tissue levels significantly increased in SCTK-MA and SCTK-AE scaffolds between two and four weeks. Though tissue in-growth into TK and PDO implants had equilibrated by four weeks (Figure 8B), the more rapid tissue infiltration facilitated by TK formulations in a fast-healing rat model suggests these materials could offer enhanced clinical benefits in slower-healing sites such as chronic wounds or critically-sized bone defects.

As demonstrated in Figure 8C, the amount of scaffold within each implant's subcutaneous site was inversely related to tissue infiltration levels. SCTK-MA, SCTK-AE, and PDO scaffolds all underwent significant biodegradation over four weeks (Figure 8C). Corresponding with in vitro degradation testing (Figure 5), SCTK-AE implants were the most substantially degraded at four weeks but did not achieve significant statistical differences from the other formulations. LCTK-MA implants also had less scaffold present at four weeks compared to two-week explants, though measured differences did not achieve statistical significance. The rapid tissue infiltration into these scaffolds may also obscure key differences in performance between TK implants and the PDO controls. As shown in prior in vitro and in vivo studies[37] and further illustrated here in Figure 5, TK materials only degrade when exposed to ROS and remain stable when ROS-generating cells are absent. It is therefore hypothesized that the ROS-producing cells which infiltrated the TK scaffolds are the main drivers of these implants' in vivo resorption (Figure 8). Though in vivo TK and PDO implant degradation was similar between two and four weeks, the hydrolysis-sensitive PDO samples would likely have experienced comparable biodegradation even without cellular in-growth. Unlike passively-degrading polyesters, these cell-triggered TK scaffolds are projected to offer significant therapeutic advantages in slow-healing tissues. In those challenging environments, TK implants are expected to maintain their structural integrity in the absence of infiltrating cells and to only undergo active resorption when activated by new tissue growth. These findings underscore the promising regenerative capabilities of these responsive 3D-printed scaffolds.

To assess cellular and tissue-level responses to the TK and PDO implants, high magnification histology images were semi-quantitatively assessed by a blinded evaluator using pathology scoring criteria listed in **Table 4**. Each image was de-identified and scored for connective tissue organization, formation of an encapsulating fibrous capsule around scaffold pieces, and the number of foreign body giant cells (FBGC). **Figure 9**A shows representative images of each implant type and the surrounding tissue response that was assessed using Table 4 scoring criteria. As shown in Figure 9B, the organization of connective tissue surrounding the TK scaffolds at the early two-week timepoint was generally more favorable than PDO implants (similar to data in

Table 4. Pathology scoring criteria.

Score	0	1	2	3
Connective tissue organization	Severe disruption of surrounding tissue	Moderate disruption of surrounding tissue	Mild disruption of surrounding tissue	No disruption
Encapsulation	Dense organized capsule formation	Tissue is highly suggestive of capsule	Early signs of encapsulation	No signs of encapsulation
Foreign body giant cells	Many	Moderate	Few	None

Figure 8B) but did not rise to a statistically significant divergence. However, by four weeks CT organization scores were statistically equivalent for all scaffolds (Figure 9B). Scores for fibrous encapsulation (Figure 9C) and foreign body giant cells (Figure 9D) were relatively consistent across scaffold types, evaluated timepoints, and animal sex (Figure S11, Supporting Information) with no significant differences seen between groups. These collective pathology scoring results demonstrate that these new TK implants promote a minimal inflammatory response that is on par with highly biocompatible PDO materials that have a long history of clinical usage.[68]

3. Conclusion

Oxidation-sensitive tissue engineering scaffolds are an emerging class of materials with exciting medical applications. Here, ROS-degradable resins that are compatible with commercial DLP 3D printers have been developed and characterized. First, easily synthesized TK precursors were generated and combined with commercially available alkene crosslinkers and photo-initiator/inhibitors to formulate AM-compatible resins. A novel small-scale resin prototyping method for screening resins' capacities for precise spatial polymerization was employed to determine optimal concentrations of photo-initiator and inhibitor

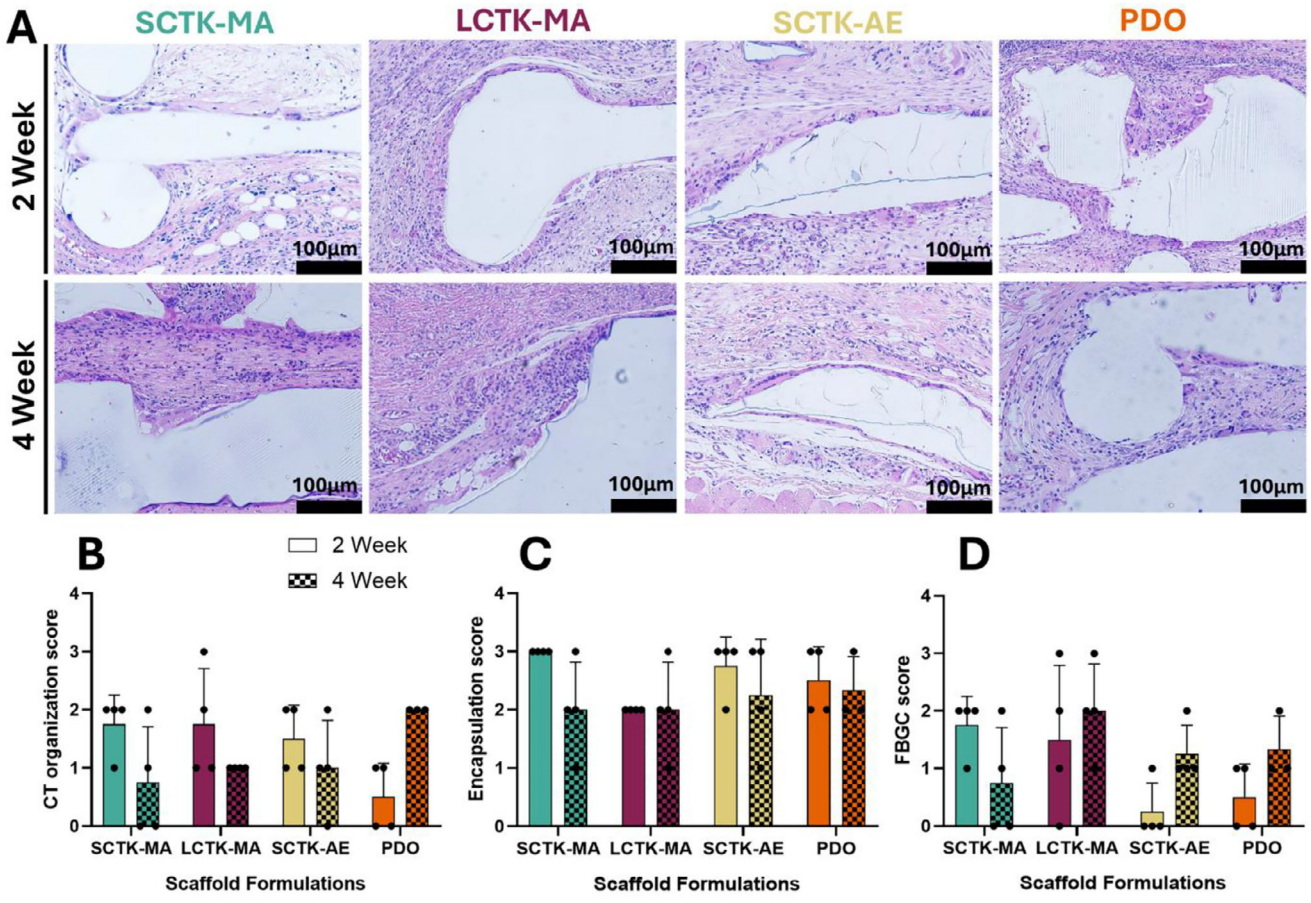

Figure 9. Tissue response analysis of implanted scaffolds as assessed from A) high magnification, H&E-stained sections of subcutaneous scaffold implants after two and four weeks. Semi-quantitative scoring of tissue sections for B) connective tissue organization, C) encapsulation of scaffold by fibrous capsule, and (D) foreign body giant cell (FBGC) presence demonstrates that TK implants promote minimal inflammation and an overall similar tissue response with commercial PDO materials.

concentrations within each formulation. An established photorheological method was employed to precisely determine the cured depth of TK resins and establish 3D printing parameters on a commercial DLP 3D printer. All optimized TK resins enabled fine-detail 3D printing of complex samples, elicited negligible in vitro cytotoxicity, and demonstrated tunable mechanical properties and oxidative sensitivity based on the resin chemistry. Lastly, 3D-printed scaffolds made from TK resins or the commercial polyester PDO were subcutaneously implanted in Sprague-Dawley rats to assess scaffold degradation and the local tissue response over four weeks. TK scaffolds underwent significant in vivo degradation over the four-week period, promoted significantly faster tissue infiltration than the commercial PDO materials, and elicited similar minimal levels of tissue inflammation as the control implants. These results demonstrate the successful creation of 3D-printable TK resins and their potential as a biomaterial platform technology that can rapidly generate oxidation-responsive, tissue-regenerating medical implants with complex architectures.

4. Experimental Section

Materials: All chemicals and materials were purchased from Fisher Scientific (Waltham, MA), except for the following. Pentaerythritol allyl ether (AE) 70% technical grade, 2,2,6,6-Tetramethylpiperidine 1-oxyl (TEMPO), and cobalt chloride ($CoCl_2$) were acquired from MilliporeSigma (St. Louis, MO). Modified essential medium α (MEMα) with no ascorbic acid, penicillin-streptomycin-glutamine (100X), and fetal bovine serum (FBS) were acquired from Gibco (Waltham, MA). The CellTiter-Glo assay kit was acquired from Promega (Madison, WI). Meloxicam Extended Release (Melox-ER) at 2 mg mL^{-1} was obtained from Wedgewood Pharmacy (Swedesboro, NJ). An Anycubic Photon Mono 4K 3D printer was purchased from Anycubic (Shenzen, China). A Prusa i3 MK3 FDM 3D printer with a FYSETC Prusa i3 Hotend MK3S J-Head extruder kit was purchased from Prusa Research (Holešovice, Czech Republic). A 50 g spool of FDM 3D printing filament (polydioxanone (PDO), trade name: Resomer X, 1.75 mm filament diameter) was purchased from Evonik (Essen, Germany). Biomed Elastic 50A Resin was obtained from Formlabs (Somerville, MA). All materials were used as received unless otherwise specified.

SCTK and LCTK Synthesis: The methods for preparation of short-chain TK (SCTK) and long-chain TK (LCTK) dithiol oligomers were adopted and optimized from Martin et. al.[37] Briefly, a stir-bar and *p*-toluenesulfonic acid monohydrate (5.6823 g) were added to a 1000 mL tri-neck round-bottom flask adapted with a 250 mL addition funnel and stopcock. The vessel was placed under high vacuum for 30 min before purging with nitrogen. For SCTK synthesis, the round-bottom flask and addition funnel were respectively charged with 300 and 100 mL of anhydrous acetonitrile. In the round-bottom flask, 180 mL (1.1 mol) of 3,6-dioxa 1,8-octanedithiol (DOT) was added. The addition funnel was then charged with 67.4 mL (0.55 mol) of 2,2-dimethoxypropane (DMP) in a 1:2 molar equivalent ratio to DOT. A molar excess of dithiol monomer was used to generate short-chain TK dimers with minimized molecular weight in the final product. For LCTK generation, the round-bottom flask and addition funnel were respectively charged with 300 mL and 150 mL of anhydrous acetonitrile. Next, 180 mL (1 mol) of DOT was added to the round-bottom flask before adding 121.3 mL (0.9 mol) of DMP to the addition funnel in a 1:0.9 molar equivalent ratio to DOT. A slight molar excess of DOT ensures final monomers are dithiol-terminated while generating a higher molecular weight product compared to the SCTK dimer. For both syntheses, the reaction vessels were then degassed with nitrogen in both the round-bottom flask and the addition funnel for 10 min. Upon completion of degassing, the DMP-acetonitrile solution was added drop-wise into the round-bottom flask with continuous stirring for 5 h. Both polymerizations were kept at room temperature (25 °C) for their duration. The reaction solutions were then transferred to 1000 mL single-neck round-bottom flasks to remove the acetonitrile via rotary evaporation. The crude SCTK and LCTK products were then purified via three rounds of precipitation in chilled volumes of 70:30 isopropanol and water.

The obtained dithiol products were analyzed via gel permeation chromatography (GPC) using poly(ethylene glycol) (PEG) dithiol molecules as standards (122–3400 Da) to estimate molecular weight. The GPC analysis was done using an Ultimate 3000 system (Thermo Fisher Scientific, Waters, MA) with a dimethylformamide (DMF) mobile phase and a Styragel HR 1 DMF column (Waters Corporation, Milford, MA). As previously described,[40] product molecular weight was also estimated using an Ellman's assay, which quantified molar thiol content per gram of material. To confirm successful polymerization and purification, the products were also dissolved in deuterated chloroform ($CDCl_3$) and analyzed with ^{1}H nuclear magnetic resonance spectroscopy (NMR, Bruker AV 400 spectrometer). ^{1}H NMR chemical shifts are reported as δ values in ppm relative to $CDCl_3$ ($\delta = 7.28$). Peak multiplicity is reported as: s(singlet), d(doublet), t(triplet), and m(multiplet). Protons representative of each peak are assigned as nH, where n represents the number of hydrogens corresponding to specific peaks based on peak integration. ^{1}H NMR: $\delta = 3.65 - 3.54$ (d, 8H), $\delta = 2.80$ (t, 2H), $\delta = 2.67$ (t, 2H), $\delta = 1.62$ (s, 1H), $\delta = 1.60$ (s, 6H).

Optimization of Photo-Initiator/Inhibitor Content in Small-Scale TK Resins: Synthesized SCTK and LCTK dithiols were combined with a photo-initiator (phenylbis(2,4,6-trimethylbenzoyl)phosphine oxide, also known as Irgacure 819 or BAPO), a photo-inhibitor (2,2,6,6-tetramethylpiperidinyl-1-oxyl, or TEMPO), and varying alkene-terminated crosslinkers (trimethylolpropane trimethacrylate (MA) or pentaerythritol allyl ether (AE) tri-functional molecules) to generate resin formulations. These three resins all featured molar equivalent matching between thiol and alkene groups from the respective TK dithiols and multi-armed crosslinkers. The three formulations are denoted as SCTK-MA (SCTK + tri-functionalized trimethylolpropane trimethacrylate), LCTK-MA (LCTK + tri-functionalized trimethylolpropane trimethacrylate), and SCTK-AE (SCTK + tri-functionalized pentaerythritol allyl ether). To note, pentaerythritol allyl ether is a nominally tetra-functionalized molecule. However, this product is specified by the supplier as containing 70% triallyl ether molecules, while the rest is a mix of diallyl and tetra-allyl ethers. Therefore, the AE crosslinker is referred to here as effectively tri-functionalized with allyl ether groups.

To augment each resin's needed amounts of photo-initiator and photo-inhibitor for achieving desired spatial printing resolutions without generating the large resin volumes needed to run a DLP printer, a small-scale rapid prototyping method was developed. Resin samples were prepared in a 5 mL scintillation vial with 1 g of SCTK or LCTK, quantities of AE or MA crosslinker to match thiol and alkene molar equivalents, 1% molar equivalent BAPO, and 0–1% molar equivalent TEMPO. Next, resins were vigorously mixed before depositing 0.1 mL of each respective formulation onto the center of a glass microscope slide ≈5 mm from the slide's top edge. Each glass slide was then placed onto the UV array of an Anycubic Photon Mono 4K DLP 3D printer with the slide's top edge aligned with the array's outer rim. This Anycubic printer possesses an outer rim UV illumination method where 10 mm of the outer UV array is illuminated for any desired amount of time. Therefore, only part of each slide's deposited resin is directly irradiated by the UV array so that the non-irradiated resin can be assessed for over-crosslinking. For each resin sample, UV illumination was engaged for 10 s and reengaged again after ≈5 s of off time to simulate layer-by-layer printing. Fifty repetitions of this process were undertaken for each resin sample. Upon completion of all simulated layers, the crosslinked resin samples on the glass slides were washed in acetone for 2 min before visually determining sample over-crosslinking in the unexposed UV areas. Resin formulations that presented minimized crosslinking in non-UV irradiated space were chosen as lead candidate formulations and carried forward in the following studies.

Formation of Bulk TK Resins for DLP 3D Printing: Three TK resins, denoted as SCTK-MA, LCTK-MA, and SCTK-AE, were formulated into bulk-

scale batches for 3D printing with an Anycubic Photon Mono 4K DLP printer. Roughly 50 mL of resin volume was needed in this 3D printer's resin bath to completely cover the build plate and generate adequate parts. To form the SCTK-MA resin batch, a magnetic stir bar was added to a 500 mL round-bottom flask, and the outside was wrapped in aluminum foil to prevent light pollution. Next, 63.9 g of SCTK (5 mol thiol content) and 36.1 g of trimethylolpropane trimethacrylate (MA, 5 mol methacrylate content) were added to the flask along with 1.34 g of BAPO (0.005 mol, 1% molar eq.) and 50 mg of TEMPO (0.0015 mol, 0.3% molar eq.). For the LCTK-MA resin, 76.3 g of LCTK (2.75 mol thiol content) and 23.7 g of MA (2.75 mol methacrylate content) were added to a 500 mL round-bottom flask along with 0.88 g BAPO (1% mol eq.) and 33 mg of TEMPO (0.3% mol. eq.). Due to the higher viscosity of LCTK, vigorous mixing using magnetic stir bars was not possible so the flask was secured to an orbital shaker table and allowed to homogenize at 200 rpm for 1h. For the SCTK-AE resin batch, 70.1 g of SCTK (5 mol thiol content) and 29.9 g of pentaerythritol allyl ether (AE, 5 mol allyl ether content) were added to the flask with 1.46 g of BAPO (0.005 mol, 1% mol. eq.) and 110 mg of TEMPO (0.001 mol, 0.2% mol. eq.). For all three resins, flasks were sealed using a 24/40 septa and mixed vigorously for 1 h. Upon completion of mixing, all resins were ready to use without further modification and were stored in 1 L UV-resistant darkroom chemical storage containers at 25 °C for up to one month between uses.

Photo-Rheology and Determination of Resin Cured Depth: Two methods for determining cured depth of the three resin batches were used in this study. Methods from Rau et al.[59] were used to precisely determine cured depth using photo-rheological methods. Briefly, 1 mL of each resin was deposited on an Anton Paar MCR 302e shear rheometer with a 25 mm aluminum parallel plate geometry on a temperature-controlled Peltier bottom plate (−20 to 180 °C). The bottom plate was made of transparent quartz to allow UV light to cure the sample from below. A thin sheet of fluorinated ethylene propylene (FEP) film was placed on top of the quartz plate to improve sample adhesion and prevent permanent curing to the quartz surface. An Omnicure LX 500 LED UV light controller was used to cure the samples in situ. A 405 nm LED head was positioned and secured below the quartz plate to illuminate the sample at an approximate distance of 10 cm. A mask was used to block excess light and illuminate the 25 mm diameter sample in the rheometer. The resin was secured between the upper and bottom plates at a gap height of 650 µm before UV illumination. The duration and intensity of the LED was externally controlled to achieve intensities (measured through the quartz and FEP film) in the range of 1–100 mW cm^{-2}. Upon completion of UV exposure, a test method was initiated to monitor gap distance and axial force while the upper plate was lowered at a constant rate of 5 µm s^{-1}. Cured thickness and UV energy was plotted on a semi log plot according to the value of the gap distance at a 2 N force threshold over 3 trials as a function of UV exposure (mJ cm^{-2}). A linear function was derived from these plots where depth of penetration (Dp) and critical exposure (Ec) was determined from each plots' slope and x-intercept, respectively. These values are used to relate cured depth (Cd) and UV exposure (E) from the Jacobs Equation (Equation 1) which are utilized as printing layer parameters. Using a Newport hand-held optical meter (Model: 1918-C) with a Newport optical power detector (Model: 918D-SL-OD3) acquired from Newport corporation (Irvine, CA), the UV energy from the Anycubic 3D printer was measured and determined to produce 1.6 mW cm^{-2}. A layer thickness of 100 µm was input into the line of best-fit for each resin and an E value was calculated. The E value in mJ cm^{-2} for each resin is divided by the 1.6 mW cm^{-2} output energy from the printer UV source to determine each resin's needed irradiation time to cure 100 µm-thick layers during 3D printing.

Evaluation of TK Resin Polymerization Conversion: A Thermo Fisher Scientific Nicollet iS50 ATR-FTIR spectrometer with smart iTX accessory was used to determine the IR spectra of TK resins before and after UV polymerization. To determine if the alkene-terminated crosslinkers were undergoing homopolymerization, the photo-initiator BAPO was mixed with the respective MA and AE constituents at a 1% molar equivalent dosage. These MA / AE + BAPO samples were deposited onto the smart iTX accessory and a 16-scan measurement was performed to establish baseline IR spectra. Next, these samples were irradiated with 405 nm light for 120 s before re-scanning and assessing the ene functional group peak (1641 cm^{-1}) before and after irradiation. To demonstrate photopolymerization of formulated TK resins and the consumption of the reactive thiol and ene groups, resin samples were scanned on the iTx to establish baseline spectra before exposing to 405 nm light for 120 s. Following UV exposure, resins were deposited onto the smart iTX accessory and scanned as described above. The characteristic thiol (2566 cm^{-1}) and ene (1641 cm^{-1}) peaks were compared before and after irradiation and used to determine functional group conversion.

Next, the Anton Paar photo-rheometer system was also used to demonstrate UV polymerization of TK resins. A time-sweep test at a constant shear rate of 10 Hz was performed on resin samples for 120 s, with UV irradiation (405 nm at 8.5 mW cm^{-2}) beginning at 30 s and storage modulus values being recorded over time. UV polymerization is demonstrated through the sharp increase in resin storage modulus after UV exposure.

TK Resin Stability Assessment via Viscometry: Since the TK dithiol constituents of these resins are degraded by free radicals, the stability of these constituents during the radical-generating 3D printing process was assessed through viscosity measurements of the TK component during UV exposure. Samples of naïve SCTK dithiol, SCTK + 1% mol. eq. BAPO, and SCTK + 1% mol. eq. BAPO + 0.3% mol. eq. TEMPO were formulated and underwent similar time-sweep tests as described above to measure viscosity over time with UV onset beginning at 30 s. These experiments were performed without the ene crosslinkers so that any decrease in SCTK viscosity (indicative of SCTK oxidative cleavage) could be detected separate from the rapid increase in sample viscosity mediated by thiol-ene photopolymerization.

To confirm the stability and lack of auto-polymerization of formulated TK resins under different storage conditions, viscosity values of freshly-made TK resins were compared against those of resins stored at room temperature (25 °C) or under refrigeration (4 °C) for 30 days. Resins from identical batches were first aliquoted into 5 mL scintillation vials and wrapped in aluminum foil to shield from light. Viscosity values of fresh resin were measured with a TA Discovery HR20 rheometer (20 mm parallel plates, 25 °C) using a shear sweep method with a shear rate range of 0–100(1/s). Resin samples of 0.1 mL volumes were deposited between the parallel plates before lowering the top plate to a gap height of 350 µm and running the shear sweep tests. The TK resins were then stored for 30 days at either 4 or 25 °C before assessing their viscosity values using the same shear sweep method. Resins stored at 4 °C were allowed to come to room temperature before testing.

Parameters and Procedures for 3D Printing using an Anycubic Photon Mono 4K DLP Printer: The Anycubic PhotonWorkshop slicer software was used to upload part files, manage resin printing parameters, and incorporate supports into 3D printed parts per the manufacturers recommended instructions. First, custom resin profiles were created in the slicer software to print with a layer thickness of 100 µm and formulation-specific layer irradiation times as determined from the cured depth experiments described above. An off-time of 4 s and 8 s was used for SCTK and LCTK resins, respectively, due to their different viscosities and flowability. To ensure part adherence to the build plate, four bottom layers (300 µm thickness each) were initially printed for all parts using an anti-alias value of 1. For each layer, a Z-lift distance of 4 mm, Z-lift speed of 0.5 mm s^{-1}, and Z retract speed of 0.5 mm s^{-1} were used when 3D printing with all three TK resins. For the Formlabs Biomed Elastic 50A resin, a layer irradiation time of 8 s was used for printing on this Anycubic 3D printer as determined from a separate cured depth experiment.

When 3D printing parts, at least 300 mL of liquid resin was added to the Anycubic printer's reservoir vat and the build plate was sanded before printing. Upon part printing completion, the build plate was removed and placed in an isopropanol-filled Anycubic Wash and Cure 2.0 system and washed for 20 min. Post-cure was performed on all parts for 60 min to ensure complete functional group conversion and breakdown of the photoinitiator. Lastly, any remaining supports or bottom adherence layers were removed from final parts using a razor blade.

Physical Characterization of 3D-Printed Parts Made from TK Resins: To measure the hydrophobicity of parts printed from the respective TK resins, water droplet contact angle measurements were collected from

fully crosslinked samples. First, a 200 µL sample of each resin was deposited onto a glass microscope slide and completely cured using the Anycubic 3D printer UV array. The hardened resin samples were then placed flat on the microscope slide and a 100 µL water drop was deposited on top of the cured resin. A goniometer using a 37MP 1080P 60FPS industrial camera from ZJchao (Shenzhen, China) was used to capture images of the water droplet on the resin surfaces and repeated for each sample type (n = 3). Measurements of the water contact angle were completed using ImageJ. To determine the molecular mesh size of the respective 3D-printed TK samples, cylinders (1 mm height × 0.5 mm diameter) were printed from the three TK resins and post-processed as described above. Samples (n = 5 per resin) were then lyophilized for 24 h, measured for their dry weights, and then submerged in 5 mL of dichloromethane (DCM) for 24h to allow solvent uptake into the polymer network. DCM-soaked cylinder weights were then recorded, and the Flory–Rehner equation[60] was used to determine network mesh size. Sol-fraction values for the respective 3D-printed TK cylinders were determined from sample dry weights (W_1) and sample dry weights after being soaked in DCM for 24 h and air drying for another 24 h (W_2). Sol-fraction values were determined using the following equation:

$$sol\ fraction = \frac{W1 - W2}{W1} \times 100\% \quad (2)$$

The tensile properties of samples 3D-printed from the three respective TK resins were assessed using standardized protocols from ASTM standard D638[63] for determining tensile properties of plastics. Briefly, type I dog-bone specimens (3.2 mm thickness, 165 mm overall length, 19 mm overall width, 13 mm neck width, 57 mm neck length) were printed from the three TK resins in a flat orientation normal to the build plate. Following printing, specimens were carefully removed, washed in isopropanol for 15 min, and post-cured for 20 min. Samples were then stored for five days in deionized (DI) water at room temperature so that "wet" mechanical properties could be determined. A TestResources universal test machine (model 100R6) with 112 lbf force transducer (model SMT2-112-294) was used to assess the tensile properties of TK resin prints (n = 5 samples per resin). Specimens were loaded onto a fixed grip possessing a deeply scored surface for adherence and prevention of slip throughout testing. A strain rate of 5 mm/min was employed during testing to collect force-displacement data, which were then converted to stress-strain curves based on the initial geometries of the respective tested samples. The elastic modulus was determined from the linear region of the stress-strain curve and calculated using the point slope formula. Yield strain and yield stress were measured at the coincidence between the stress-strain curve and a 2% offset line in the elastic deformation region. Toughness was measured as the area under the stress-strain curve until ultimate failure using the trapezoid method.

To confirm these new TK resins could be used to 3D print parts with complex geometries, "Benchy" tugboat STL models were downloaded from grabCAD and uploaded into Anycubic PhotonWorkshop for slicing. Medium-density supports were added, which were automatically determined by the software.

In Vitro Degradation of 3D-Printed TK Samples: To assess the in vitro degradation of parts 3D-printed from the SCTK-MA, LCTK-MA, and SCTK-AE resins, cylindrical samples with a 1 mm height and 0.5 mm diameter were printed, washed, and post-cured as described above. Respective samples were incubated in one of three degradation media, including non-oxidative phosphate-buffered saline (PBS), highly oxidative media comprising DI water with 20% mass percentage hydrogen peroxide (H_2O_2) and 0.1 M cobalt chloride ($CoCl_2$), and less oxidative 2% H_2O_2 in 0.01 M $CoCl_2$. Cobalt ions react with the H_2O_2 in the oxidative media to stimulate the formation of highly reactive hydroxyl radicals.[64] For all degradation studies, printed samples were weighed before placing them in 2 mL microcentrifuge tubes and assigned a future collection timepoint with n = 3 replicates. Respective degradation media were then added to each tube (1 mL volume) to completely submerge each sample before incubating on a shaker table at 37 °C for up to 35 days. Upon timepoint completion, samples were removed and washed thoroughly in DI water and dried for 48h before recording their final mass. Finally, scaffold samples from all three formulations that had been incubated in PBS or 20% H_2O_2 for 3 days were assessed for compressive mechanical properties. Samples were placed between parallel plates on an Anton Paar MCR 302e rheometer, exposed to compressive loading at a linear deformation rate of 10 µm s^{-1} until sample break or the maximum loading of 40 N. The response was converted into stress–strain data based on the sample dimensions, and the compressive modulus was determined from the slope of the curve's linear region at low strain

In Vitro Cytotoxicity of Samples Printed from TK Resins: All cell culture experiments were carried out using MC3T3-E1 pre-osteoblast cells (American Type Culture Collection, ATCC) incubated under sterile conditions at 37 °C with 5% CO_2. Media for these cells used a base MEMα (no ascorbic acid) supplemented with 10% FBS and 1% penicillin/streptomycin. In vitro cytotoxicity of 3D-printed cylinder samples from the three TK resins was assessed using an elution assay following protocols outlined in ISO 10993-5. TK cylinders were printed from all resins with a 1 × 0.5 mm height and diameter. A biostable Biomed Elastic 50A resin was also used to print analogous cylinder samples as a commercially available material control. Before use, all cylinders were washed in isopropanol for 15 min, post-cured for 20 min, allowed to air dry overnight, and then autoclaved to sterilize. Printed samples were then weighed before being placed in a volume of cell media to give a ratio of 100 mg sample mass per 1 mL of media. Scaffold samples were incubated at 37 °C for 24 h before sterile filtering the conditioned media using 0.2 µm cellulose acetate membrane filters. MC3T3-E1 cells were seeded in a 96 well plate (0.01×10^6 cells/well) for 24 h and then treated with 100 µL of serially-diluted conditioned media from the printed cylinders using n = 3 seeded wells per treatment. Full unmodified media was used as a control and diluent. A CellTiter-Glo assay was used to assess the number of viable cells per treatment.

Design and Printing of Grid-Architecture Scaffolds from TK Resins and PDO Filaments: Highly porous tissue engineering scaffolds were modeled using SolidWorks 2024 SP2.0. The parts were designed with overall dimensions of 10.6 mm (length) by 10.6 mm (width) by 0.800 mm (thickness) in overall profile, and were constructed from 0.2 mm-thick struts stacked in alternating patterns. This strut configuration generated square pores of 600 µm length by 600 µm width which were interconnected by 200 µm-thick channels. The designed part had a volume of 25 mm^3, a surface area of 434.4 mm^2, and a total bounding volume of 89.9 mm^3 as calculated using the SolidWorks "Mass Properties Tool". Porosity of these scaffolds was calculated at 72% using the equation below.

$$Porosity\ (\%) = \frac{\left(Volume_{total} - Volume_{scaffold}\right)}{Volume_{total}} \times 100 \quad (3)$$

To print these grid scaffolds with micron-scale features, the TK resins were modified to slightly adjust concentrations of TEMPO to prevent over-crosslinking and maintain open pore geometries in final constructs. These modified resin constituents are listed in Table S2 (Supporting Information). The slightly modified resin constituents necessitated slightly different print parameters (Table S3, Supporting Information) on the Anycubic system generate these small-feature scaffolds. Final resin prints were removed from the build plate with a razor blade and post-processed using the protocols described above.

Polydioxanone (PDO) was chosen as a control material for these experiments due to its commercial availability, hydrolytic degradation, and quick degradation timeline compared to other commercially available alternatives such as PCL and PLGA. To 3D print the PDO filament (Resomer X from Evonik), a Prusa i3 MK3 FDM printer was utilized. The machine was outfitted with a FYSETC Prusa i3 Hotend MK3S J-Head extruder kit (24 V, 40 W for 1.75 mm direct filament extrusion) and a 0.2 mm diameter E3 nozzle. Prusa Slicer Version 2.8.0 software was used for file conversion and printing control. Most of the manufacturer-supplied settings for a Prusa i3 MK3 with a 0.25 mm nozzle were used for part printing. However, key parameter alterations were as follows: Print Settings: Layer & First Layer Height = 0.17 mm, Perimeters = 1, Seam Position = Aligned, Print Speed = 20%; Filament Settings: Diameter = 1.75 mm, Density = 1.328 g cm^{-3},

Nozzle Temperature = 185 °C, Bed Temperature = 40 °C; Machine/Printer Settings: Nozzle Diameter = 0.17 mm. After the machine's first layer calibration and test printing, the design and slicing software settings enabled the machine to print entire samples in one continuous extrusion, ensuring minimal artifacts/defects and high accuracy + reproducibility for FDM printing. These samples were removed from the build plate using a razor blade and packaged for later sterile processing. To visualize the final parts, the generated TK and PDO implants were imaged using a digital light microscope (VHX-1000 by KEYENCE) from a top view at 20x and 100x.

Efficacy Analysis of 3D-Printed Grid-Architecture Scaffolds: For the analysis of printed scaffold tolerances, grid scaffolds from all four formulations (SCTK-MA, LCTK-MA, SCTK-AE, and PDO; $n = 3$ samples per group) were positioned between two glass microscope slides to ensure flatness before imaging with a Nikon Eclipse Ti2 inverted microscope equipped with a Nikon DS-Qi2 camera. Image acquisition and measurements were performed using Nikon NIS-Elements software (version 5.30.05). Each captured image included three replicate scaffolds per print condition. Within each image, strut width measurements from five intact square pores were obtained. Specifically, the top and left walls of each square were measured three times (once at each end and once at the center) using the NIS-Elements built-in measurement tool. This approach yielded 30 strut width measurements per scaffold and 120 measurements for each formulation. For analysis, measurements of struts were considered technical replicates, and individual scaffolds were considered biological replicates within their respective groups. Strut width measurements from the 3D printed scaffolds were imported from a CSV file and processed using a custom Python script. Descriptive statistics (mean ± standard deviation) were computed at the individual scaffold and sample type levels to evaluate differences in mean strut width across scaffold formulations.

In Vivo Subcutaneous Implantation: All animal studies were approved by the University of Cincinnati Institutional Animal Care and Use Committee (IACUC) and are documented in IACUC protocol # 22-04-22-01. Procedures for the subcutaneous implantation of 3D-printed scaffolds (SCTK-MA, LCTK-MA, SCTK-AE, and PDO formulations) followed previously reported methods.[37] First, the three crosslinked TK scaffold formulations were sterilized via autoclave. Since the PDO samples were fabricated from a thermoplastic non-crosslinked polymer, they could not be sterilized by autoclave and were instead soaked in pure ethanol for 24 h before being sterilized with UV for 30 min on each side in a sterile biosafety cabinet. Briefly, 8-week-old Sprague-Dawley rats ($n = 3$ female and $n = 3$ male for each time point) acquired from Charles River Laboratories (Charleston, SC) were anesthetized using isoflurane, shaved using electric clippers, and the skin prepared using betadine and 70% ethanol. Rats were administered a pre-operative dose of melox-ER at 2.0 mg kg^{-1}. Next, a small 0.5 cm incision was created through the ventral skin mid-abdomen on each rat before separating the skin from the underlying muscle and fascia using dull surgical scissors. Each rat received $n = 6$ scaffold implants in their subcutaneous space, and the placement location for each scaffold formulation was randomized to limit any site-specific effects on healing outcomes (implant placement schematic given in Figure S10, Supporting Information). Following implant placement, the skin incision was closed using three interrupted stitches with VeterSut 4-0 polyglactin sutures. Half the animal cohort was euthanized at two weeks post-implantation to harvest scaffold/tissue samples, and the other half were similarly euthanized at four weeks post-implantation for sample collection.

Histological Analysis: Following euthanasia, skin and abdominal tissues surrounding the six separate implanted scaffolds were extracted and partitioned. While most scaffolds were successfully recovered, some did not generate quantifiable tissue explants sufficient for analysis and were excluded. Tissue samples were placed in individual vials and fixed in 10% (vol/vol) of formalin for 3 days. Upon completion of fixation, the tissue extracts were bisected and embedded with the cross-section of the implant site facing downward to enable visualization of the interior areas of the scaffolds. Paraffin-embedded tissue blocks were serially cut in 5 µm sections and stained with hematoxylin and eosin (H&E) for tissue visualization.

Quantification of tissue infiltration and scaffold degradation for respective implants was performed using a custom Python image segmentation script (code provided in Supporting Information) utilizing the OpenCV python library. All images used in this analysis were taken using a PathScan Enabler 5 (Meyer Instruments Inc., Houston TX) slide scanner with 10000 DPI resolution. High magnification images of tissue sections were taken using an Olympus IX83 microscope (Tokyo, Japan) and stitched together using Olympus analysis software. Semi-quantitative scoring of the tissue response for de-identified tissue sections was performed by a blinded evaluator using a scoring system adapted from Brown et al.[72] to assess connective tissue organization, encapsulation of scaffold materials in a fibrous capsule, and the presence of foreign body giant cells. Scoring criteria for each tissue attribute are given in Table 4 and have possible scores ranging from 0 to 3.

Statistical Analysis: The data presented here are reported as mean and standard deviation of the mean. For data featuring continuous variables, statistical analyses for comparing two groups were performed using a Student's t-test. Statistical analyses for multiple group comparisons were performed using one way analysis of variance (ANOVA), including a Tukey's post-hoc test. For non-normally distributed data sets, a non-parametric Kruskal–Wallis test was used for multiple group comparisons. A post-hoc Dunn's test was done with p-values adjusted using Bonferroni's method to find which groups were significantly different. For all statistical tests, p-values less than 0.05 were considered to be statistically significant.

Supporting Information

Supporting Information is available from the Wiley Online Library or from the author.

Acknowledgements

This work was supported by the University of Cincinnati (UC) Office of Research, the Department of Defense Congressionally Directed Medical Research Programs (grant # W81XWH-22-1-0075), and the National Institutes of Health (grant # R21DE031391 and R01NS134804). Additionally, R.L.D. was supported in part by the National Institute for Occupational Safety and Health through the University of Cincinnati Education and Research Center (grant # T42OH008432). The authors would also like to thank Dr. Jonathan Pham and Ms. Kyujin Ko for assistance using their goniometer.

Conflict of Interest

The authors declare no conflict of interest.

Data Availability Statement

The data that support the findings of this study are available in the supplementary material of this article.

Keywords

3D printing, biomaterials, digital light processing, reactive oxygen species

Received: August 22, 2025
Revised: November 6, 2025
Published online: November 20, 2025

[1] A. Khademhosseini, R. Langer, *Nat. Protoc.* **2016**, *11*, 1775.

[2] K. V. Wong, H. Aldo, *ISRN Mech Eng* **2012**, *2012*, 1.
[3] P. Szymczyk-Ziółkowska, M. B. Łabowska, J. Detyna, I. Michalak, P. Gruber, *Biocybern. Biomed. Eng.* **2020**, *40*, 624.
[4] A. J. T. Teo, A. Mishra, I. Park, Y.-J. Kim, W.-T. Park, Y.-J. Yoon, *ACS Biomater. Sci. Eng.* **2016**, *2*, 454.
[5] D. Fan, Y. Li, X. Wang, T. Zhu, Q. Wang, H. Cai, W. Li, Y. Tian, Z. Liu, *Front. Pharmacol.* **2020**, *11*, 1.
[6] L. Zhang, G. Yang, B. N. Johnson, X. Jia, *Acta Biomater.* **2019**, *84*, 16.
[7] F. P. W. Melchels, J. Feijen, D. W. Grijpma, *Biomaterials* **2010**, *31*, 6121.
[8] M. Alizadeh-Osgouei, Y. Li, C. Wen, *Bioact. Mater.* **2019**, *4*, 22.
[9] C. Yu, J. Schimelman, P. Wang, K. L. Miller, X. Ma, S. You, J. Guan, B. Sun, W. Zhu, S. Chen, *Chem. Rev.* **2020**, *120*, 10695.
[10] S. Wasti, S. Adhikari, *Front. Chem.* **2020**, *8*, 1.
[11] K. Tappa, U. Jammalamadaka, D. H. Ballard, T. Bruno, M. R. Israel, H. Vemula, J. M. Meacham, D. K. Mills, P. K. Woodard, J. A. Weisman, *PLoS One* **2017**, *12*, 1.
[12] J. A. Weisman, J. C. Nicholson, K. Tappa, U. Jammalamadaka, C. G. Wilson, D. Mills, *Int. J. Nanomedicine* **2015**, *10*, 357.
[13] J.-H. Shim, J.-Y. Won, J.-H. Park, J.-H. Bae, G. Ahn, C.-H. Kim, D.-H. Lim, D. W. Cho, W. S. Yun, E. B. Bae, C.-M. Jeong, J. B. Huh, *Int. J. Mol. Sci.* **2017**, *18*, 889.
[14] L. Dong, S.-J. Wang, X.-R. Zhao, Y.-F. Zhu, J.-K. Yu, *Sci. Rep.* **2017**, *7*, 4.
[15] C. R. Almeida, T. Serra, M. I. Oliveira, J. A. Planell, M. A. Barbosa, M. Navarro, *Acta Biomater.* **2014**, *10*, 613.
[16] S. Shen, H. Wang, Y. Xue, L. Yuan, X. Zhou, Z. Zhao, E. Dong, B. Liu, W. Liu, B. Cromeens, B. Adler, G. Besner, R. X. Xu, *Sci. Rep.* **2017**, *7*, 1.
[17] J. J. Huang, J.-A. Ren, G.-F. Wang, Z. A. Li, X.-W. Wu, H.-J. Ren, S. Liu, *World J. Gastroenterol.* **2017**, *23*, 7489.
[18] H. O. T. Ware, R. Hai, C. Sun, *Vat Photopolymerization* **2023**, *F1592*.
[19] S. C. Ligon, R. Liska, J. Stampfl, M. Gurr, R. Mülhaupt, *Chem. Rev.* **2017**, *117*, 10212.
[20] M. Pagac, J. Hajnys, Q.-P. Ma, L. Jancar, J. Jansa, P. Stefek, J. Mesicek, *Polymers (Basel)* **2021**, *13*, 1.
[21] Y. Bao, N. Paunović, J.-C. Leroux, *Adv. Funct. Mater.* **2022**, *32*, 2109864.
[22] L. N. Woodard, M. A. Grunlan, *ACS Macro Lett.* **2018**, *7*, 976.
[23] C. Engineer, J. Parikh, A. Raval, *Trends Biomater. Artif. Organs* **2011**, *25*, 79.
[24] D. Hofmann, M. Entrialgo-Castaño, K. Kratz, A. Lendlein, *Adv. Mater.* **2009**, *21*, 3237.
[25] J. E. Dumas, E. M. Prieto, K. J. Zienkiewicz, T. Guda, J. C. Wenke, J. Bible, G. E. Holt, S. A. Guelcher, *Tissue Eng Part A* **2013**, *20*, 115.
[26] B. A. Badeau, C. A. DeForest, *Annu. Rev. Biomed. Eng.* **2019**, *21*, 241.
[27] R. J. Mondschein, A. Kanitkar, C. B. Williams, S. S. Verbridge, T. E. Long, *Biomaterials* **2017**, *140*, 170.
[28] M. Shafiq, Y. Chen, R. Hashim, C. He, X. Mo, X. Zhou, *Front Bioeng. Biotechnol.* **2021**, *9*, 1.
[29] J. R. Martin, C. L. Duvall, *Oxidative Stress and Biomaterials*, Elsevier, Amsterdam **2016**, pp. 225.
[30] A. Phaniendra, D. B. Jestadi, L. Periyasamy, *Indian J. Clin. Biochem.* **2015**, *30*, 11.
[31] V. Jaenen, S. Fraguas, K. Bijnens, M. Heleven, T. Artois, R. Romero, K. Smeets, F. Cebrià, *Sci. Rep.* **2021**, *11*, 1.
[32] M. A. Chelombitko, *Moscow. Univ. Biol. Sci. Bull.* **2018**, *73*, 199.
[33] A. J. Sheppard, A. M. Barfield, S. Barton, Y. Dong, *Front. Bioeng. Biotechnol.* **2022**, *10*, 1.
[34] M. Mittal, M. R. Siddiqui, K. Tran, S. P. Reddy, A. B. Malik, *Antioxidants Redox Signal* **2014**, *20*, 1126.
[35] N. I. Md Fadilah, S. J. Phang, N. Kamaruzaman, A. Salleh, M. Zawani, A. Sanyal, M. Maarof, M. B. Fauzi, *Antioxidants* **2023**, *12*, 787.
[36] D. S. Wilson, G. Dalmasso, L. Wang, S. V. Sitaraman, D. Merlin, N. Murthy, *Nat. Mater.* **2010**, *9*, 923.
[37] J. R. Martin, M. K. Gupta, J. M. Page, F. Yu, J. M. Davidson, S. A. Guelcher, C. L. Duvall, *Biomaterials* **2014**, *35*, 3766.
[38] M. A P McEnery, S. Lu, M. K Gupta, K. J. Zienkiewicz, J. C. Wenke, K. N. Kalpakci, D. Shimko, C. L. Duvall, S. A. Guelcher, *RSC Adv.* **2016**, *6*, 109414.
[39] M. A. P. McGough, L. A. Boller, D. M. Groff, J. G. Schoenecker, J. S. Nyman, J. C. Wenke, C. Rhodes, D. Shimko, C. L. Duvall, S. A. Guelcher, *ACS Biomater. Sci. Eng.* **2020**, *6*, 564.
[40] R. L. Dos Santos, A. Ahmed, B. E. Hunn, A. E. Addison, D. W. Marques, K. A. Brucea, J. R. Martin, *Biomater. Sci.* **2025**, *13*, 1975.
[41] J. R. Martin, C. E. Nelson, M. K. Gupta, F. Yu, S. M. Sarett, K. M. Hocking, A. C. Pollins, L. B. Nanney, J. M. Davidson, S. A. Guelcher, C. L. Duvall, *Adv. Healthcare Mater.* **2016**, *5*, 2751.
[42] M. T. Howard, S. Wang, A. G. Berger, J. R. Martin, S. Jalili-Firoozinezhad, R. F. Padera, P. T. Hammond, *Biomaterials* **2022**, *288*, 121721.
[43] A. Mohamed, Z. Jun, G. Quan, Z. W. A, L. Ji, G. Jin, *ACS Appl. Polym. Mater* **2022**, *4*, 7812.
[44] J. R. Martin, P. Patil, F. Yu, M. K. Gupta, C. L. Duvall, *Biomaterials* **2020**, *263*, 120377.
[45] P. Patil, K. A. Russo, J. T. McCune, A. C. Pollins, M. A. Cottam, B. R. Dollinger, C. R. DeJulius, M. K. Gupta, R. D'Arcy, J. M. Colazo, F. Yu, M. G. Bezold, J. R. Martin, N. L. Cardwell, J. M. Davidson, C. M. Thompson, A. Barbul, A. H. Hasty, S. A. Guelcher, C. L. Duvall, *Sci. Transl. Med.* **2022**, *14*, eabm6586.
[46] B. H. Northrop, R. N. Coffey, *J. Am. Chem. Soc.* **2012**, *134*, 13804.
[47] W. Rutsch, K. Dietliker, D. Leppard, M. Köhler, L. Misev, U. Kolczak, G. Rist, *Prog. Org. Coatings* **1996**, *27*, 227.
[48] A. Urrios, C. Parra-Cabrera, N. Bhattacharjee, A. M. Gonzalez-Suarez, L. G. Rigat-Brugarolas, U. Nallapatti, J. Samitier, C. A. DeForest, F. Posas, J. L. Garcia-Corderob, A. Folch, *Lab Chip* **2016**, *16*, 2287.
[49] J. E. Boulden, N. B. Cramer, K. M. Schreck, C. L. Couch, C. Bracho-Troconis, J. W. Stansbury, C. N. Bowman, *Dent. Mater.* **2011**, *27*, 267.
[50] E. Yoshida, *Polymers (Basel)* **2012**, *4*, 1125.
[51] D. Ahn, L. M. Stevens, K. Zhou, Z. A. Page, *Adv. Mater.* **2021**, *33*, 1.
[52] M. Mołoń, D. Szlachcikowska, K. Stępień, P. Kielar, S. Galiniak, *Biochim. Biophys. Acta-Mol. Cell Res.* **2023**, *1870*, 119412.
[53] M. Dzwonkowska-Zarzycka, A. Sionkowska, *Molecules* **2024**, *29*, 3898.
[54] A. Schwab, R. Levato, M. D'Este, S. Piluso, D. Eglin, J. Malda, *Chem. Rev.* **2020**, *120*, 11028.
[55] C. E. Hoyle, C. N. Bowman, *Angew. Chemie Int Ed* **2010**, *49*, 1540.
[56] G. J. Domski, J. M. Rose, G. W. Coates, A. D. Bolig, M. Brookhart, *Prog. Polym. Sci.* **2007**, *32*, 30.
[57] P. F. Jacobs, *Rapid Prototyping & Manufacturing: Fundamentals Of Stereolithography*, 1st ed. Society of Manufacturing Engineers, Southfield, MI, USA **1992**.
[58] J. Choi, R. B. Wicker, S. Cho, C. Ha, S. Lee, *Rapid Prototyp. J.* **2009**, *15*, 59.
[59] D. A. Rau, J. P. Reynolds, J. S. Bryant, M. J. Bortner, C. B. Williams, *Addit. Manuf.* **2022**, *60(PA)*, 103207.
[60] S. D. Bruck, *J. Res. Natl. Bur. Stand Sect A Phys. Chem.* **1961**, *65A*, 485.
[61] M. M Gad, S. M. Fouda, *J. Prosthodont* **2023**, *32*, 96.
[62] D. W. L. Hukins, J. C. Leahy, K. J. Mathias, *J. Mater. Chem.* **1999**, *3*, 629.
[63] American Society for Testing and Materials, *ASTM Stand.* **2014**, *08*, 1.
[64] M. A. Schubert, M. J. Wiggins, J. M. Anderson, A. Hiltner, *J. Biomed. Mater. Res.* **1997**, *34*, 519.
[65] J. R. Martin, M. T. Howard, S. Wang, A. G. Berger, P. T. Hammond, *Adv. Healthc. Mater.* **2021**, *10*, 2001941.
[66] H. F. Mukasheva, L. Adilova, A. Dyussenbinov, B. Yernaimanova, M. Abilev, D. Akilbekova, *Front. Bioeng. Biotechnol.* **2024**, *12*, 1.
[67] G. Lutzweiler, A. Ndreu Halili, N. Engin Vrana, *Pharmaceutics* **2020**, *12*, 602.

[68] J. A. Stramiello, A. Mohammadzadeh, J. Ryan, M. T. Brigger, *Int. J. Pediatr Otorhinolaryngol* **2020**, *139*, 110405.
[69] M. Yang, L. Chu, Y. Zhuang, C. Qi, S. Meng, Z. Liu, T. Kong, *Adv. Funct. Mater.* **2024**, *34*, 2316456.
[70] S. M. Montgomery, F. Demoly, K. Zhou, H. J. Qi, *Adv. Funct. Mater.* **2023**, *33*, 2213252.
[71] C. C. Cook, E. J. Fong, J. J. Schwartz, D. H. Porcincula, A. C. Kaczmarek, J. S. Oakdale, B. D. Moran, K. M. Champley, C. M. Rackson, A. Muralidharan, R. R. McLeod, M. Shusteff, *Adv. Mater.* **2020**, *32*, 2003376.
[72] B. N. Brown, R. Londono, S. Tottey, L.i Zhang, K. A. Kukla, M. T. Wolf, K. A. Daly, J. E. Reing, S. F. Badylak, *Acta Biomater.* **2012**, *8*, 978.